

Independently Tunable Flat Bands and Correlations in a Graphene Double Moiré System

Yimeng Wang¹, Jihang Zhu², G. William Burg¹, Anand Swain³, Kenji Watanabe⁴, Takashi Taniguchi⁵,
Yuebing Zheng³, Allan H. MacDonald², and Emanuel Tutuc^{1,*}

¹*Microelectronics Research Center Department of Electrical and Computer Engineering
The University of Texas at Austin Austin Texas 78758 USA*

²*Department of Physics University of Texas at Austin Austin Texas 78712 USA*

³*Walker Department of Mechanical Engineering Texas Materials Institute The University of Texas at Austin
Austin Texas 78712 USA*

⁴*Research Center for Functional Materials National Institute of Materials Science
1-1 Namiki Tsukuba Ibaraki 305-0044 Japan*

⁵*International Center for Materials Nanoarchitectonics National Institute of Materials Science
1-1 Namiki Tsukuba Ibaraki 305-0044 Japan*

Received 10 September 2024; revised 27 November 2024; accepted 21 January 2025; published 7 March 2025)

We report on a double moiré system consisting of four graphene layers, where the top and bottom pairs form small-twist-angle bilayer graphene, and the middle interface has a large rotational mismatch. This system shows clear signatures of two sets of spatially separated flat bands associated with the top and bottom twisted bilayer graphene subsystems, each independently tunable. Thermodynamic analysis reveals weak correlations between bilayers that allow the chemical potential to be measured as a function of carrier density for each constituent TBG. We find that correlated insulating states at integer number of electrons per moiré unit cell are most robust near magic angle, whereas gapped states at neutrality are more robust at larger twist angles.

DOI: [10.1103/PhysRevLett.134.096204](https://doi.org/10.1103/PhysRevLett.134.096204)

Materials with extremely flat energy bands have attracted great scientific interest due to quenched electron kinetic energy that leads to strong electron correlations. The theoretical discovery and experimental realization of flat bands in magic-angle twisted bilayer graphene (MATBG) [1–3] have opened up paths to engineered flat-band materials. Subsequent studies have revealed the intricacy of electronic correlations in twisted bilayer graphene (TBG) flat bands with various correlated phases, including ferromagnetism [4,5], Chern insulators [6,7], strange metal states [8,9], etc., all of which reside in MATBG's rich phase diagram. The ongoing debate on the interplay between correlated insulating and superconducting phases in MATBG may help uncover the origin of unconventional superconductivity [10–13]. Besides TBG, tunable flat bands in multilayer graphene moiré systems have been explored, including alternating twisted multilayer graphene [14–19] and twisted $m+n$ layer graphene [20–24]. Here, we report the experimental realization of a double moiré system in which two independent TBG moiré bands are placed in proximity. By stacking two TBGs with a relatively large rotational mismatch we weaken hybridization between constituent TBGs, leading to approximate particle number conservation in each TBG. Our approach

illustrates a method to experimentally realize quantum confined flat bands in a multilayer homostructure using exclusively twist control. Remarkably, the constituent TBGs display correlated insulators at integer number of electrons per moiré unit cell near magic angle, which shows that intramoiré interactions remain strong despite the proximity of the other TBG. By utilizing the unique combination of compressible and incompressible states in the two TBGs we extract the chemical potential as a function of carrier density in the constituent TBGs. Furthermore, we find that gaps at neutrality in individual TBGs are stronger away from the magic angle regime, pointing to a qualitative difference between many-electron physics away from vs at magic angle.

The moiré system in this study consists of four graphene monolayers, with two controlled twist angles (0.91° – 1.57°)—the twist angle between the top two layers (θ_T), and between the bottom two layers (θ_B). The twist angle between the middle layers is not controlled and intentionally kept large ($> 5^\circ$) [Figs. 1 a) and 1 b)]. The double moiré samples are dual-gated [Fig. 1 a) inset] with hexagonal boron nitride (hBN) as gate dielectric, and the channels are etched into a Hall bar [Fig. 1 c)]. Data from four samples, labeled S1–S4 are discussed in the Letter. The large twist angle between the middle graphene layers suppresses electron tunneling by shifting their K valleys in the momentum space.

*Contact author: etutuc@mail.utexas.edu

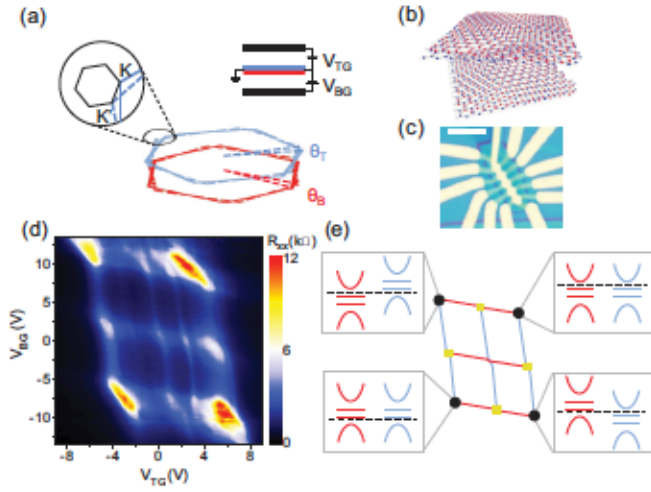


FIG. 1. a) Brillouin zones of the top (blue) and bottom (red) TBG in the double moiré system. Inset shows the biasing scheme for the dual-gated sample. b) Schematic of the double moiré lattice formed by four graphene monolayers. The top two graphene monolayers are shifted vertically for clarity. c) Optical micrograph of a double moiré sample. The scale bar is 5 μm . d) R_{xx} vs V_{TG} and V_{BG} measured in sample S1 at $T = 95$ mK. e) Schematic of the resistance peaks pattern seen in d). The black dots mark the four most prominent peaks associated with the moiré band fillings depicted in the band diagrams of the top (blue) and bottom (red) TBGs. Black dashed line represents the Fermi level. Yellow squares mark the peaks when one of the TBG is charge neutral. Blue (red) lines mark the constant density loci for top (bottom) TBG when tracing incompressible states.

Thus, tunneling contributes at high order in perturbation theory and acts as a contribution to disorder.

Figure 1 d) shows the longitudinal resistance (R_{xx}) as a function of top (V_{TG}) and bottom (V_{BG}) gate biases measured in a double moiré sample with $\tau = 1.7^\circ$ and $\beta = 1.38^\circ$ (sample S1). The most prominent resistance peaks are located at the corners of the contour plot, marked by the black dots in Fig. 1 e). At the midpoint of each two adjacent peaks, additional local resistance maxima are marked by yellow squares in Fig. 1 e). We associate these resistance peaks with the integer filling states per valley and spin of the top and bottom TBG moiré bands. For example, the upper left peak [upper left black dot in Fig. 1 e)] corresponds to the insulating state where the top TBG flat bands are empty and the bottom TBG fully filled. Similarly, the bottom peak around $V_{TG} = 1$ V [bottom yellow square in Fig. 1 e)] corresponds to the state where the top TBG flat bands are charge neutral and the bottom TBG empty. Noticeably, in Fig. 1 d), there are local resistance maxima connecting the resistance peaks with moderate resistance values higher than the background [blue and red lines in Fig. 1 e)], which can be associated with the integer filling of either top (blue) or bottom (red) TBG moiré bands. Additional local resistance maxima extending along the y-axis direction around $V_{TG} = 3$ V are a signature of

correlated insulating state in the flat bands of the top TBG. The data in Fig. 1 d) provide evidence for two spatially separated, independently tunable flat bands. They demonstrate that electronic confinement in multilayer graphene stacks can be compactly realized by changing the twist angles, in contrast to traditional band engineering that employs dissimilar materials.

We treat the double moiré as a system consisting of two layers with separately conserved particle numbers that are mutually correlated. The relation between the gate biases and the chemical potentials is then [25]

$$\begin{aligned} V_{BG}C_{BG} &= en_B + \frac{\mu_B}{e}(C_{BG} + C_{IL}) - \frac{\mu_T}{e}C_{IL}, \\ V_{TG}C_{TG} &= en_T + \frac{\mu_T}{e}(C_{TG} + C_{IL}) - \frac{\mu_B}{e}C_{IL}. \end{aligned} \quad (1)$$

Here, e is the elementary charge, C_{TG} and C_{BG} are the areal capacitances of the top and bottom gates, respectively. The two TBG subsystems are assumed to be electrostatically coupled by an areal capacitance C_{IL} . The carrier densities in the top and bottom TBG subsystems are n_T and n_B , respectively, and $\mu_X = e(n_T, n_B)/n_X$ ($X = T, B$) is the chemical potential in layer X . This expression fully accounts for intralayer and interlayer correlation contributions to the energy per area $\epsilon(n_T, n_B)$. According to Eq. 1), if μ_T and n_T (μ_B and n_B) are kept constant, the change in the (V_{TG}, V_{BG}) reflects the change in μ_B (μ_T). Similar double layer systems have been previously utilized to probe the chemical potential of two-dimensional electron systems, albeit with an interlayer barrier and external interlayer bias [29–32].

The TBG subsystems in the double moiré system have both compressible and incompressible states. A charge gap (incompressibility) in layer X results in a cusp in the dependence of ϵ on n_X and a corresponding jump discontinuity in μ_X [Fig. 2 a)]. Figure 2 b) illustrates the (V_{TG}, V_{BG}) gate voltage ranges over which the subsystem is incompressible in the top (orange) and bottom (green) TBG; the incompressible states are labelled by the moiré band filling factors at which the chemical potential jumps occur. We define the filling factors $\nu_{T,B} = n_{T,B}/n_{sT,sB}$, where $n_{sT,sB} = (8/3)(\tau_{T,B}/a)^2$, with $a = 2.46$ Å the graphene lattice constant, are respectively the carrier densities required to fill one moiré Brillouin zone of the top or bottom TBG, including its four-fold spin and valley degeneracy. Quarter-multiple filling factors correspond to integer numbers of particles per moiré unit cell. Note that a state that is incompressible in one or both TBGs corresponds to a segment, or diamond respectively in the (V_{TG}, V_{BG}) plane. The black dashed rectangle in Fig. 2 b) marks a diamond where the ground state is incompressible in both layers [Fig. 2 c)]. Along its boundaries, the chemical potential in one layer is fixed at one edge of its chemical potential jump interval in its incompressible

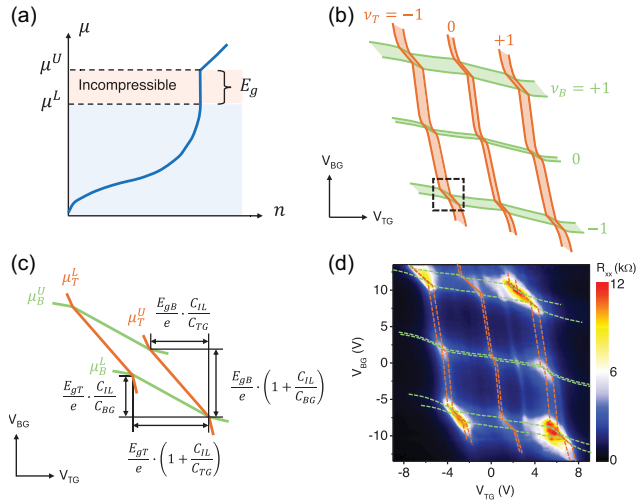


FIG. 2. a) μ vs n of a system displaying finite compressibility for $\mu < \mu^L$ (blue shaded region), and an incompressible state for $\mu^L < \mu < \mu^U$ (pink shaded region) with a gap $E_g = \mu^U - \mu^L$. b) Schematic of the incompressible states of the top (orange) and bottom (green) TBG subsystems seen in the R_{xx} vs V_{TG} and V_{BG} plot. The black dashed rectangle marks a diamond-shaped region where both TBGs are in incompressible states. c) Expanded view of the dashed black rectangle in panel b). The diamond dimensions are determined by the incompressible state gaps. d) R_{xx} vs V_{TG} and V_{BG} data in Fig. 1 e) showing the constant μ_T and μ_B lines at the edge of incompressible states.

state [Fig. 2 a)]. Using Eq. 1) the diamond dimensions along the V_{TG} and V_{BG} axes can be readily related to the incompressible state gaps. For example, when μ_B varies between the incompressible state interval at constant μ_T :

$$\begin{aligned} \Delta V_{BG} &= \frac{E_{gB}}{e} \left(1 + \frac{C_{IL}}{C_{BG}} \right), \\ \Delta V_{TG} &= \frac{E_{gB}}{e} \frac{C_{IL}}{C_{TG}} \end{aligned} \quad (2)$$

Here, E_{gB} is the size of the bottom TBG gap, ΔV_{BG} and ΔV_{TG} are the gate bias changes needed to move the Fermi level across the gap. Corresponding equations can be written for the top TBG gap by keeping μ_B constant. Since the slopes of the diamond edges are determined only by the capacitance values, the interlayer capacitance C_{IL} can be determined [25]. We extract $C_{IL} = 1.6 \text{ F/cm}^2$, a value corresponding to two parallel plates separated by 0.55 nm vacuum, comparable to distance between the midplanes of the TBG subsystems.

When correlations between TBG subsystems are negligible, the chemical potential in each TBG depends only on its own density and the analysis simplifies. For example, at constant μ_T and hence n_T) Eq. 1) implies that

$$\begin{aligned} \Delta \mu_B &= e \Delta V_{TG} \frac{C_{TG}}{C_{IL}}, \\ \Delta n_B &= \frac{1}{e} \left[\Delta V_{BG} C_{BG} + \Delta V_{TG} C_{TG} \left(1 + \frac{C_{BG}}{C_{IL}} \right) \right] \end{aligned} \quad (3)$$

According to Eq. 3), on a constant μ_T trace, each point in the (V_{TG}, V_{BG}) plane can be converted into a μ_B and a corresponding n_B value, rendering the μ_B vs n_B relation. We exploit the property that the μ_T values at the edges of gaps are easily identified experimentally by sharp changes in resistance. Because there are several incompressible states as the filling factor varies, multiple constant μ_T loci are traceable in a R_{xx} vs (V_{TG}, V_{BG}) map. We observe identical μ_B vs n_B μ_T vs n_T) dependence at all integer ν_T (ν_B) values, justifying the weak-correlation assumption which allows us to use one layer to probe the other at least when one layer is incompressible.

By analyzing the R_{xx} vs (V_{TG}, V_{BG}) data [Fig. 2 d)] in a double moiré sample, the relations μ vs n for both constituent TBGs can be determined [25]. In Fig. 3 a), the chemical potential of a constituent TBG close to the magic angle is plotted as a function of carrier density and moiré band filling factor (top axis). We observe jumps near half fillings $\nu = \pm 1/2$ which we associate with broken flavor symmetry states induced by strong electron interactions [31,33,34]. The jumps occur concomitantly with the correlated insulators in constituent TBG flat bands. The shaded areas mark the gap sizes calculated with Eq. 2) in the incompressible states with filling factors $\nu = \pm 1$. The carrier densities at these full-filling states are converted into the twist angle. Figures 3 b) 3 d) summarize μ vs ν with the twist angle ranging from 0.91° to 1.57° measured in four double moiré samples (labeled S1-S4), as well as the gap sizes at the integer fillings $E_{g,v}$ and the change of the chemical potential over the filling factor ranges from $1 < \nu < \Delta\mu_p$) and $< \nu < 1 - \Delta\mu_n$). In Figs. 3 c) and 3 d), we compare our results with previously reported chemical potential measurements [31,33-36], most of which were studied near magic angle.

Our study provides μ vs n data in the TBG flat bands over a wide range, and is in good agreement with previous studies near magic angle [31,33-36]. As we see in Fig. 3 b), the chemical potential dependence on filling factor is consistently weaker for TBGs with larger than the magic angle, suggesting flatter moiré bands on the hole side compared to the electron side. Surprisingly, we see in Fig. 3 c) that the gap sizes at $\nu =$ show a minimum near the magic angle, and increase with away from the magic angle. Gaps at neutrality are not observed in most MATBG experiments [31,33-35,37], except in rare cases where the sample has minimal strain [38]. Conversely, gaps at quarter multiples of moiré Brillouin zone fillings are only observed near the magic angle, and are associated with flavor polarization in ultraflat bands. The qualitative difference between the twist angle dependencies of the gaps at

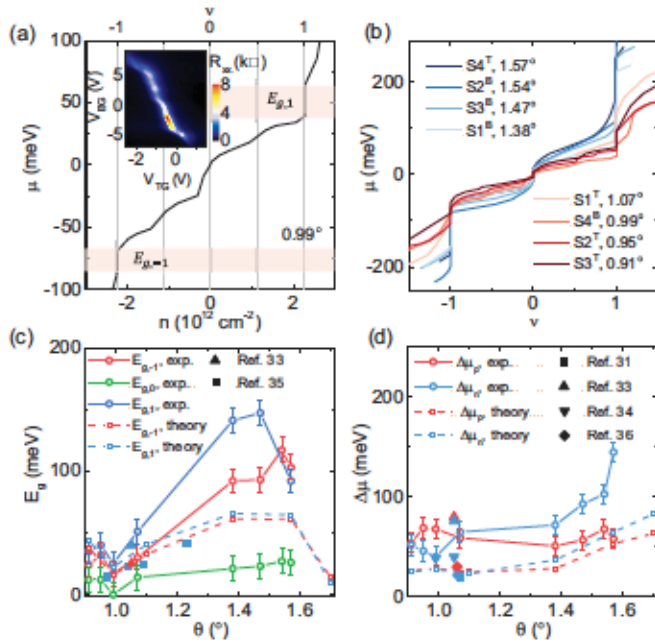


FIG. 3. a) μ vs n in a 0.99° TBG, measured in a double moiré sample with $\nu_T = 1.57^\circ$ and $\nu_B = .99^\circ$ sample S4). The shaded areas mark the incompressible states with $\nu_B = \pm 1$. Inset shows R_{xx} vs V_{TG} and V_{BG} around $\nu_T = 0$. The peak depicts the constant μ_T loci at $\nu_T = 0$. b) μ vs n for TBGs with varying θ , extracted from four samples. The superscripts label the constituent top (T) and bottom (B) TBGs. c) $E_{g,v}$ vs θ . d) $\Delta\mu_p$ and $\Delta\mu_n$ vs θ . Scattered symbols are data from literature. Red (blue) symbols denote valence (conduction) side of the band. Data from Ref. [34] in d) are measured in 12T parallel magnetic field.

neutrality vs those at quarter-multiple filling factors suggests that the former originate from a different type of broken symmetry, perhaps similar to the flavor-dependent layer polarization states [39–42] that are thought to produce gaps in suspended Bernal bilayer graphene between valence and conduction bands for each flavor [43]. We note that our experimental data cannot rule out that TBG remains a semi-metal at neutrality, but if so it would have to have an interaction-reshaped Fermi velocity that is significantly larger compared to the band value [25]. The $\Delta\mu_n$ ($\Delta\mu_p$) data which measure the bandwidth of the conduction (valence) flat bands, show large electron-hole asymmetry in the band flatness, especially for large twist angles. Furthermore, on the valence side of the flat band, the change in the chemical potential has a weaker dependence on the twist angle compared to the conduction side.

We compare our experimental data with the predictions of a self-consistent Hartree approximation that are summarized by the dashed lines in Figs. 3 c) and 3 d). The use of this approximation is justified by the fact that correlations are expected to be weak when the flat bands are empty and when they are full [44]. To qualitatively match the observed variations in insulating gaps across different twist angles,

we set $\alpha = .3$ for $\theta = .91^\circ$, $\alpha = .6$ for $\theta = .99^\circ$ to 1.57° and $\alpha = 1$ for $\theta = 1.7^\circ$, where α is the ratio between same and different sublattice interlayer tunneling and is introduced as a phenomenological parameter [25]. The dependence of α on the twist angle can be qualitatively attributed to the corrugation effect, which becomes more pronounced at smaller twist angles, leading to a smaller α for smaller twist angles. Additionally, we included a nonlocal interlayer tunneling term [44,45] to qualitatively capture the electron-hole asymmetry in the band structure. The nonlocal interlayer tunneling strength is defined as $w_{NL} = t b_M / A_{uc}$, where $t = dt_k / dk$ at the graphene Dirac point, t_k is the Fourier transform of the two-center approximation of the interlayer hopping amplitude $t(\mathbf{r})$, b_M is the moiré reciprocal lattice vector length, and A_{uc} is the moiré unit cell area. For simplicity, we used a constant $w_{NL} = 2$ meV in Figs. 3 c) and 3 d), but note that the rigorous value of w_{NL} should be twist angle dependent and experimentally determined. The calculations of $E_{g,\pm 1}$ and $\Delta\mu_{p,n}$ agree well with experimental measurements. Specifically, $E_{g,\pm 1}$ increases with twist angle before an abrupt drop near $\theta \sim 1.57^\circ$, and a noticeable dip near the magic angle. These features of $E_{g,\pm 1}$ are directly influenced by the varying α values at these twist angles. $\Delta\mu_{p,n}$ show minimal dependence on twist angle for $\theta \lesssim 1.38^\circ$ followed by a visible increase as bandwidths increase for $\theta \gtrsim 1.38^\circ$. The value we have chosen for the constant w_{NL} results in a smaller electron-hole asymmetry in the calculation. From the definition of w_{NL} above, w_{NL} should be larger for larger twist angles (assuming weak dependence of t on twist angle in the small range explored in our experiment). We expect, therefore, larger electron-hole asymmetry at larger twist angles that is not captured by our constant- w_{NL} approximation. The larger $E_{g,\pm 1}$ and $\Delta\mu_{p,n}$ in our experimental data compared to the Hartree approximation results are due to contributions from exchange interactions and correlations.

Figure 4 a) shows a contour plot of R_{xx} as a function of V_{TG} and V_{BG} in a sample with $\nu_T = 1.57^\circ$ and $\nu_B = .99^\circ$ measured at $T = 95$ mK. The most prominent resistance peaks around $V_{TG} = \pm 8$ V signal that the top TBG is incompressible with $\nu_T = \pm 1$. Figure 4 b) focuses on the resistance peaks with $\nu_T = 1$. Multiple insulating states associated with integer fillings $\nu_B = 0, 1$ and correlated insulators at quarter-multiple fillings $\nu_B = \pm \frac{1}{2}, \frac{3}{4}$ are observed. In Fig. 4 c) the insulating behavior of the correlated insulators is confirmed by temperature-dependence measurements. Similar correlated insulators with the same ν_B values are present with $\nu_T = 1$ as well. We observe signatures of correlated insulators in all the TBG subsystems close to the magic angle down to 0.91° [25]. This observation suggests that the proximity of one TBG does not suppress the correlated insulating states in the other TBG, even though screening suggests the possibility [12].

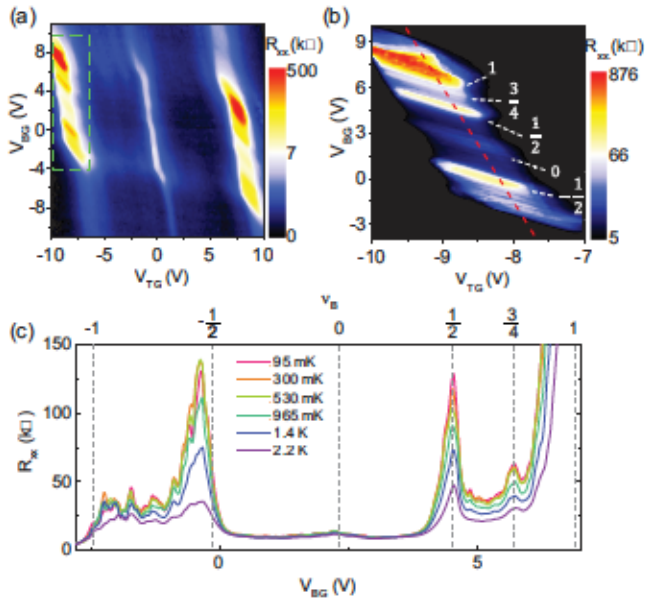


FIG. 4. a) R_{xx} vs V_{TG} and V_{BG} measured in sample S4 with $\tau = 1.57^\circ$ and $B = .99^\circ$ at $T = 95$ mK. b) Expanded view of the data in the green dashed rectangle in panel a). The ν_B values corresponding to the resistance peaks are included, highlighting correlated insulators at $\nu_B = \pm \frac{1}{2}$ and $\frac{3}{4}$. c) Temperature dependence of R_{xx} vs V_{BG} measured along the red dashed line in b). The top axis shows ν_B .

We note that superconductivity is not observed in our double moiré samples down to the base temperature of our dilution refrigerator (95 mK), even though they show clear correlated insulators. This observation is interesting in light of theoretical interest in the relationship between superconducting and flavor orders in MATBG. Since superconducting phases are usually accompanied by correlated phases with spin or valley order at nearby filling factors similar to high-temperature superconductors [46], the two phases are sometimes assumed to arise from a common mechanism. However, experimental studies have also shown that superconductivity can be present when the correlated insulators are suppressed [9,11,12]. Furthermore, in MATBG, the superconducting phase is experimentally observed to be more robust on the valence bands [2,4,10]. As our measurements show that the valence bands are flatter than the conduction counterpart, these findings suggest that a flatter band is favorable for superconductivity, either directly through a higher density of states or indirectly by suppressing other competing states that inhibit superconductivity. Meanwhile, the substrate has also been shown to impact the critical temperature of the superconducting phase in both TBG and twisted double bilayer graphene [13,47]. In the double moiré system studied here, each TBG is bound by hBN on one side, and the opposite TBG on the other, distinctly different from the case of hBN encapsulated MATBG. This difference in environment may suppress superconductivity in our samples.

We demonstrated a double moiré system with spatially separated, independently tunable flat moiré bands. The unique combination of compressible and incompressible states in constituent TBGs that are weakly correlated enables the extraction of the chemical potential vs carrier density relationship in each TBG subsystem. We find that correlation induced gaps at neutrality and at nonzero filling factors have an entirely distinct dependence on twist angle, and that the moiré bands are marked by strong electron-hole asymmetry in which the valence bands are flatter than the conduction bands.

Acknowledgments The work at The University of Texas at Austin was supported by the National Science Foundation (NSF) Grants No. MRSEC DMR-2308817, and No. EECS-2122476; Army Research Office under Grant No. W911NF-22-1-2; and the Welch Foundation Grant No. F-2169-20230405. J.Z. and A. H. M. acknowledge support from Department of Energy grant DE-SC0019481. A. S. and Y.Z. acknowledge support from NSF Grant No. 2140985.

- [1] R. Bistritzer and A. H. MacDonald, *Proc. Natl. Acad. Sci. U.S.A.* **108**, 12233 (2011).
- [2] Y. Cao, V. Fatemi, S. Fang, K. Watanabe, T. Taniguchi, E. Kaxiras, and P. Jarillo-Herrero, *Nature (London)* **556**, 43 (2018).
- [3] Y. Cao, V. Fatemi, A. Demir, S. Fang, S. L. Tomarken, J. Y. Luo, J. D. Sanchez-Yamagishi, K. Watanabe, T. Taniguchi, E. Kaxiras, R. C. Ashoori, and P. Jarillo-Herrero, *Nature (London)* **556**, 80 (2018).
- [4] X. Lu, P. Stepanov, W. Yang, M. Xie, M. A. Aamir, I. Das, C. Urgell, K. Watanabe, T. Taniguchi, G. Zhang, A. Bachtold, A. H. MacDonald, and D. K. Efetov, *Nature (London)* **574**, 653 (2019).
- [5] A. L. Sharpe, E. J. Fox, A. W. Barnard, J. Finney, K. Watanabe, T. Taniguchi, M. A. Kastner, and D. Goldhaber-Gordon, *Science* **365**, 605 (2019).
- [6] K. P. Nuckolls, M. Oh, D. Wong, B. Lian, K. Watanabe, T. Taniguchi, B. A. Bernevig, and A. Yazdani, *Nature (London)* **588**, 610 (2020).
- [7] Y. Xie, A. T. Pierce, J. M. Park, D. E. Parker, E. Khalaf, P. Ledwith, Y. Cao, S. H. Lee, S. Chen, P. R. Forrester, K. Watanabe, T. Taniguchi, A. Vishwanath, P. Jarillo-Herrero, and A. Jacoby, *Nature (London)* **600**, 439 (2021).
- [8] Y. Cao, D. Chowdhury, D. Rodan-Legrain, O. Rubies-Bigorda, K. Watanabe, T. Taniguchi, T. Senthil, and P. Jarillo-Herrero, *Phys. Rev. Lett.* **124**, 076801 (2020).
- [9] A. Jaoui, I. Das, G. Di Battista, J. Díez-Mérida, X. Lu, K. Watanabe, T. Taniguchi, H. Ishizuka, L. Levitov, and D. K. Efetov, *Nat. Phys.* **18**, 633 (2022).
- [10] M. Yankowitz, S. Chen, H. Polshyn, Y. Zhang, K. Watanabe, T. Taniguchi, D. Graf, A. F. Young, and C. R. Dean, *Science* **363**, 1059 (2019).
- [11] Y. Saito, J. Ge, K. Watanabe, T. Taniguchi, and A. F. Young, *Nat. Phys.* **16**, 926 (2020).

- [12] P. Stepanov, I. Das, X. Lu, A. Fahimniya, K. Watanabe, T. Taniguchi, F. H. L. Koppens, J. Lischner, L. Levitov, and D. K. Efetov, *Nature London* **583**, 375 (2020).
- [13] H. S. Arora, R. Polski, Y. Zhang, A. Thomson, Y. Choi, H. Kim, Z. Lin, I. Z. Wilson, X. Xu, J.-H. Chu, K. Watanabe, T. Taniguchi, J. Alicea, and S. Nadj-Perge, *Nature London* **583**, 379 (2020).
- [14] G. Chen, L. Jiang, S. Wu, B. Lyu, H. Li, B. L. Chittari, K. Watanabe, T. Taniguchi, Z. Shi, J. Jung, Y. Zhang, and F. Wang, *Nat. Phys.* **15**, 237 (2019).
- [15] G. Chen, A. L. Sharpe, P. Gallagher, I. T. Rosen, E. J. Fox, L. Jiang, B. Lyu, H. Li, K. Watanabe, T. Taniguchi, J. Jung, Z. Shi, D. Goldhaber-Gordon, Y. Zhang, and F. Wang, *Nature London* **572**, 215 (2019).
- [16] J. M. Park, Y. Cao, K. Watanabe, T. Taniguchi, and P. Jarillo-Herrero, *Nature London* **590**, 249 (2021).
- [17] J. M. Park, Y. Cao, L.-Q. Xia, S. Sun, K. Watanabe, T. Taniguchi, and P. Jarillo-Herrero, *Nat. Mater.* **21**, 877 (2022).
- [18] G. W. Burg, E. Khalaf, Y. Wang, K. Watanabe, T. Taniguchi, and E. Tutuc, *Nat. Mater.* **21**, 884 (2022).
- [19] Y. Zhang, R. Polski, C. Lewandowski, A. Thomson, Y. Peng, Y. Choi, H. Kim, K. Watanabe, T. Taniguchi, J. Alicea, F. von Oppen, G. Refael, and S. Nadj-Perge, *Science* **377**, 1538 (2022).
- [20] G. W. Burg, J. Zhu, T. Taniguchi, K. Watanabe, A. H. MacDonald, and E. Tutuc, *Phys. Rev. Lett.* **123**, 197702 (2019).
- [21] X. Liu, Z. Hao, E. Khalaf, J. Y. Lee, Y. Ronen, H. Yoo, D. Haei Najafabadi, K. Watanabe, T. Taniguchi, A. Vishwanath, and P. Kim, *Nature London* **583**, 221 (2020).
- [22] S. Chen, M. He, Y.-H. Zhang, V. Hsieh, Z. Fei, K. Watanabe, T. Taniguchi, D. H. Cobden, X. Xu, C. R. Dean, and M. Yankowitz, *Nat. Phys.* **17**, 374 (2021).
- [23] S. Xu, M. M. Al Ezzi, N. Balakrishnan, A. Garcia-Ruiz, B. Tsim, C. Mullan, J. Barrier, N. Xin, B. A. Piot, T. Taniguchi, K. Watanabe, A. Carvalho, A. Mishchenko, A. K. Geim, V. I. Fal'ko, S. Adam, A. H. C. Neto, K. S. Novoselov, and Y. Shi, *Nat. Phys.* **17**, 619 (2021).
- [24] D. Waters, E. Thompson, E. Arreguin-Martinez, M. Fujimoto, Y. Ren, K. Watanabe, T. Taniguchi, T. Cao, D. Xiao, and M. Yankowitz, *Nature London* **620**, 750 (2023).
- [25] See Supplemental Material at <http://link.aps.org/supplemental/10.1103/PhysRevLett.134.096204> which includes Refs. [26–28], for additional information about the experimental methods and theoretical calculations.
- [26] M. Koshino, N. F. Q. Yuan, T. Koretsune, M. Ochi, K. Kuroki, and L. Fu, *Phys. Rev. X* **8**, 031087 (2018).
- [27] J. Kang and O. Vafek, *Phys. Rev. B* **107**, 075408 (2023).
- [28] O. Vafek and J. Kang, *Phys. Rev. B* **107**, 075123 (2023).
- [29] S. Kim, I. Jo, D. C. Dillen, D. A. Ferrer, B. Fallahzad, Z. Yao, S. K. Banerjee, and E. Tutuc, *Phys. Rev. Lett.* **108**, 116404 (2012).
- [30] K. Lee, B. Fallahzad, J. Xue, D. C. Dillen, K. Kim, T. Taniguchi, K. Watanabe, and E. Tutuc, *Science* **345**, 58 (2014).
- [31] J. M. Park, Y. Cao, K. Watanabe, T. Taniguchi, and P. Jarillo-Herrero, *Nature London* **592**, 43 (2021).
- [32] Y. Wang, J. Herzog-Arbeitman, G. W. Burg, J. Zhu, K. Watanabe, T. Taniguchi, A. H. MacDonald, B. A. Bernevig, and E. Tutuc, *Nat. Phys.* **18**, 48 (2022).
- [33] D. Wong, K. P. Nuckolls, M. Oh, B. Lian, Y. Xie, S. Jeon, K. Watanabe, T. Taniguchi, B. A. Bernevig, and A. Yazdani, *Nature London* **582**, 198 (2020).
- [34] U. Zondiner, A. Rozen, D. Rodan-Legrain, Y. Cao, R. Queiroz, T. Taniguchi, K. Watanabe, Y. Oreg, F. von Oppen, A. Stern, E. Berg, P. Jarillo-Herrero, and S. Ilani, *Nature London* **582**, 203 (2020).
- [35] Y. Choi, J. Kemmer, Y. Peng, A. Thomson, H. Arora, R. Polski, Y. Zhang, H. Ren, J. Alicea, G. Refael, F. von Oppen, K. Watanabe, T. Taniguchi, and S. Nadj-Perge, *Nat. Phys.* **15**, 1174 (2019).
- [36] J. Yu, B. A. Foutty, Z. Han, M. E. Barber, Y. Schattner, K. Watanabe, T. Taniguchi, P. Phillips, Z.-X. Shen, S. A. Kivelson, and B. E. Feldman, *Nat. Phys.* **18**, 825 (2022).
- [37] M. Oh, K. P. Nuckolls, D. Wong, R. L. Lee, X. Liu, K. Watanabe, T. Taniguchi, and A. Yazdani, *Nature London* **600**, 240 (2021).
- [38] K. P. Nuckolls, R. L. Lee, M. Oh, D. Wong, T. Soejima, J. P. Hong, D. Cálugáru, J. Herzog-Arbeitman, B. A. Bernevig, K. Watanabe, T. Taniguchi, N. Regnault, M. P. Zaletel, and A. Yazdani, *Nature London* **620**, 525 (2023).
- [39] H. Min, G. Borghi, M. Polini, and A. H. MacDonald, *Phys. Rev. B* **77**, 041407 R (2008).
- [40] R. T. Weitz, M. T. Allen, B. E. Feldman, J. Martin, and A. Yacoby, *Science* **330**, 812 (2010).
- [41] J. Velasco Jr, L. Jing, W. Bao, Y. Lee, P. Kratz, V. Aji, M. Bockrath, C. Lau, C. Varma, R. Stillwell *et al.*, *Nat. Nanotechnol.* **7**, 156 (2012).
- [42] A. H. MacDonald, J. Jung, and F. Zhang, *Phys. Scr.* **2012**, 014012 (2012).
- [43] W. Bao, J. Velasco, F. Zhang, L. Jing, B. Standley, D. Smirnov, M. Bockrath, A. H. MacDonald, and C. N. Lau, *Proc. Natl. Acad. Sci. U.S.A.* **109**, 10802 (2012).
- [44] J. Zhu, I. Torre, M. Polini, and A. H. MacDonald, *Phys. Rev. B* **110**, L121117 (2024).
- [45] M. Xie and A. H. MacDonald, *Phys. Rev. Lett.* **127**, 196401 (2021).
- [46] B. Keimer, S. A. Kivelson, M. R. Norman, S. Uchida, and J. Zaanen, *Nature London* **518**, 179 (2015).
- [47] R. Su, M. Kuri, K. Watanabe, T. Taniguchi, and J. Folk, *Nat. Mater.* **22**, 1332 (2023).